# PMDSPH: A Hybrid $N$-Body and SPH Code and Its Application to the Milky Way

ROGER FUX
Research School of Astronomy and Astrophysics, Australian National University, Mount Stromlo Observatory,
Cotter Road, Weston ACT 2611, Australia
E-mail: fux@mso.anu.edu.au

## ABSTRACT

PMDSPH is a combined 3D particle-mesh and SPH code aimed to simulate the self-consistent dynamical evolution of spiral galaxies including live stellar and collisionless dark matter components, as well as an isothermal gas component. This paper describes some aspects of this code and shows how its application to the Milky Way helps to recover the gas flow within the Galactic bar region from the observed HI and CO longitude-velocity distributions.

*Key Words* : methods: $N$-body simulation – hydrodynamics – Galaxy: structure – ISM: kinematics and dynamics

## I. INTRODUCTION

The 3D PMDSPH code is a substantially modified version of Friedli's (1992) PMSPH code, which itself is a merging of a particle-mesh (PM) $N$-body code using a polar-cylindrical grid (Pfenniger & Friedli 1993) and a Smooth Particle Hydrodynamical (SPH) code developed by Willy Benz. The main original features of the present code are (i) the passage from a single gravitational grid to a double grid geometry, allowing to increase the resolution in the disc region of the spirals to be modelled, (ii) the way the smoothing lengths of the SPH particles are updated at each time step, (iii) the algorithm to find the closest neighbours to each SPH particle, and (iv) the replacement of the Runge-Kutta-Fehlberg time integrator by a "synchronised" leap-frog. Sections I to IV are devoted to a description of the code, merely focusing on those points.

In the last decade, the evidence that the Milky Way is a barred galaxy has become overwhelming. The presently most quoted values for the main parameters of the bar are an inclination angle of its major axis relative to the Sun-centre line $\varphi = 15° - 45°$, with the near end of the bar pointing in the first Galactic quadrant, and a corotation radius $R_{\rm CR} = 3.5 - 5$ kpc (see Gerhard 2001 for a recent review). Several groups have tried to model the gas kinematics implied by such a bar. Section V shortly summarises the results obtained in this respect using our PMDSPH code. More details can be found in Fux (1999).

## II. GRAVITATION

The gravitational potential is related to the mass density $\rho(\vec{r})$ through the Poisson integral, which in polar-cylindrical coordinates writes:

$$\Phi(R,\phi,z) = -G\int_0^\infty R'dR \int_0^{2\pi} d\phi' \int_{-\infty}^\infty dz'\rho(R',\phi',z')\cdot$$
$$K(R,R',|\phi-\phi'|,|z-z'|), \quad (1)$$

where:

$$K(...) \equiv \frac{1}{\sqrt{R^2+R'^2-2RR'\cos(\phi-\phi')+(z-z')^2}} \quad (2)$$

is the Keplerian kernel. The $\phi$ and $z$ integrals are convolutions which can be efficiently calculated by fast Fourier transform (FFT) using the convolution theorem (note that the Keplerian kernel does not truly satisfy the conditions of this theorem, but the softened kernel adopted in the code does). The integration over $R$ must be done by directly.

Our code derives the potential on polar-cylindrical grids. Hereafter, we first consider the case of a single grid, for which more details can be found in Pfenniger & Friedli (1993), and then extend to the double grid.

### (a) Single grid

To apply the FFT in $\phi$ and $z$, a constant vertical ($H_z$) and azimuthal spacing of the grid cells is required. The radial distribution of the cells is free and taken as logarithmic with a linear core to avoid an accumulation point at the centre:

$$R_j = R_{\max} \frac{\exp\left[j/(\frac{1}{2}+\frac{N_\phi}{2\pi})\right]-1}{\exp\left[N_R/(\frac{1}{2}+\frac{N_\phi}{2\pi})\right]-1}, \quad j = 0,..,N_R, \quad (3)$$

where $R_{\max}$ is the maximum radial extent of the grid. This choice ensures that the cells are nearly square-shaped in the $x - y$ plane over a large radial range. The number of cells is $(N_R + 1) \times N_\phi \times (N_z + 1)$. The advantage of this grid over Cartesian grids when simulating spiral galaxies is that the azimuthal and radial resolutions increase towards the centre.

The potential is softened using a variable homogeneous ellipsoidal kernel with semi principal-axes parallel to the $R$, $\phi$ and $z$ directions and matched to the local cell dimensions (see Fig. 1).

The mass assignment is achieved by distributing the mass of each particle to the height nearest grid

points according to the *Cloud in Cell* method (CIC, Hockney & Eastwood 1981). With the substitution $dM = \rho R\, dR'\, d\phi'\, dz'$ and transforming into finite sums, equation (1) becomes:

$$\Phi_{i_R,i_\phi,i_z} = -G \sum_{j_R=0}^{N_R} X_{i_R,j_R,i_\phi,i_z}, \qquad (4)$$

$$X_{i_R,j_R,i_\phi,i_z} \equiv \sum_{j_\phi=1}^{N_\phi} \sum_{j_z=0}^{N_z} M_{j_R,j_\phi,j_z} K_{i_R,j_R,i_\phi-j_\phi,i_z-j_z}, \qquad (5)$$

where $M_{j_R,j_\phi,j_z}$ is the total mass assigned to the grid cell indexed $(j_R, j_\phi, j_z)$. The discrete version of the convolution theorem then leads to:

$$[\hat{X}_{i_R,j_R}]_{k_\phi,k_z} = [\hat{M}_{j_R}]_{k_\phi,k_z} \cdot [\hat{K}_{i_R,j_R}]_{k_\phi,k_z}, \qquad (6)$$

and

$$[\hat{\Phi}_{i_R}]_{k_\phi,k_z} = G \sum_{j_R=0}^{N_R} [\hat{X}_{i_R,j_R}]_{k_\phi,k_z}, \qquad (7)$$

where the hats stand for the 2D Fourier transform in $\phi$ and $z$. The potential finally results as the inverse Fourier transform of $[\hat{\Phi}_{i_R}]_{k_\phi,k_z}$.

The kernel is not symmetric in $i_R$ and $j_R$. Its Fourier transform is computed only once in the beginning of the simulation and then stored in memory. To optimise the FFT, $N_\phi$ and $(N_z + 1)$ must be a multiple of small prime factors. Only the part of the grid from $j_z = 1$ to $N_z/2$ is used for the mass assignment ("active" grid). The other part, with $M_{j_R,j_\phi,j_z} = 0$, is added to kill the periodic images of the potential (*doubling-up* method, see Hockney & Eastwood 1981). The plane $j_z = 0$ provides the necessary potential for the evaluation of the vertical forces at $j_z = 1$. Note that in Fux (1999), $N_z$ is defined as half this parameter here.

The accelerations are first calculated at the grid points by finite differentiation and then interpolated to the particle positions by inverse CIC. For the particles outside the active grid, the acceleration is approximated assuming that the total mass of the system is confined at the centre. A drawback of the PM method is that the position of the centre of mass (CM) is exponentially unstable. This problem is suppressed by subtracting the position $\vec{r}_{CM}$ and velocity of the CM to the phase-space coordinates of the particles every time when $|\vec{r}_{CM}| > D_{lim} = 10^{-4}$ kpc.

## (b) Double grid

A single grid with constant $H_z$ fails to model efficiently the high density contrast between a thin disc and an extended halo (lots of cells waisted in $z$). Therefore, a second lower resolution grid (B) is added to the original grid (A), as illustrated in Fig. 1, with grid
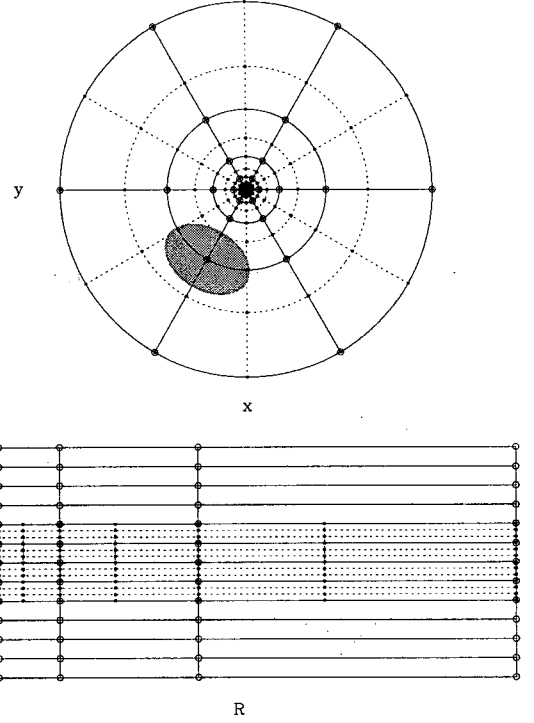


**Fig. 1.**— Example of a double grid with $N_R = 10$, $N_\phi = 12$, $N_z/2 = 13$ and $M_z = 3$. The solid points and dotted lines are the points and meshes of grid A, and the circles and solid lines those of grid B. Only the active parts of the grids are represented. The top frame also shows the projection of the gravitational kernel within one cell.

points defined as:

$$R_i^B = R_{2i}^A, \qquad i = 0,\ldots,N_R/2, \qquad (8)$$

$$\phi_j^B = \phi_{2(j-1)+1}, \qquad j = 1,\ldots,N_\phi/2, \qquad (9)$$

$$z_k^B = \left[k - \frac{N_z/2+1}{2}\right] M_z H_z, \quad k = 0,\ldots,N_z. \qquad (10)$$

Grid B has half the number of cells in $R$ and $\phi$, skipping every second point of grid A in these dimensions, and the same number of cells in $z$ but with a spacing of $M_z H_z$. Its radial size is as grid A, but $z_{max}^B = M_z z_{max}^A$. Both grids have constant spacing in $\phi$ and $z$, allowing to keep the advantage of the FFT algorithm in those dimensions. $N_R$ and $N_\phi$ must be even and the vertical grid parameters are chosen to satisfy $N_z/2 = 1 + 2lM_z$, $l$ integer $\geq 2$, ensuring that (i) there are grid points of each grid in the plane $z = 0$, (ii) the horizontal planes $z = \pm z_{max}^A$ delimitating the active part of grid A also contain points of grid B, and (iii) grid B has at least four cells within grid A in the $z$ dimension.

The mass assignment is done twice (once for each grid), and the total potential involves the evaluation of three sub-potentials: $\Phi_A$, $\Phi_B$ and $\Phi_C$, respectively due to the mass within grid A, the mass within grid B,

and the mass within the part of grid B outside grid A. The sub-potential $\Phi_A$ is the only one computed at high resolution on grid A. The total potential then amounts to $\Phi_A + \Phi_C$ in the region of grid A, and simply to $\Phi_B$ outside this region. The increase of CPU time owing to the triple potential evaluation is largely compensated by the reduction by a factor $\sim M_z$ of the effective number of cells relative to a single grid with the same resolution as grid A and the same size as grid B. The small force discontinuities at the vertical boundaries of the active part of grid A are linearly smoothed out within the region $z_{\max}^A - M_z H_z \leq |z| \leq z_{\max}^A$.

## III. SPH

We will not discuss here the details of the SPH technique (see for instance Benz 1990 and Monaghan 1992 for reviews), but rather start by noting the following. The PMDSPH code assumes an isothermal perfect-gas equation of state, i.e. $P = c_s^2/\gamma \cdot \rho$ with a sound speed $c_s$ constant in space and time. In particular, there is no energy equation involved in the code, and the adiabatic index $\gamma$ and $c_s$ play a degenerate role. The adopted SPH kernel is a spherically symmetric spline that vanishes outside two smoothing lengths. The gravity of the gas particles is included and calculated exactly as for the other collisionless particles.

The next two subsections describe how the smoothing lengths are handled by the code and present the algorithm used for the search of neighbouring particles.

### (a) Smoothing length updating

The gas particles are given individual smoothing lengths $h_i$ in a way such that the number of neighbours $N_i$ to each particle always remains as close as possible to a constant number $N_o$, allowing to increase the spatial resolution in high density regions like shocks.

At each time step, the $h_i$'s are updated considering the 3D scaling law:

$$\frac{h_i}{h_o} = \left( \frac{N_i + 1}{N_o + 1} \frac{\rho_o}{\rho_i} \right)^{1/3}, \qquad (11)$$

where $h_o$ and $\rho_o$ are constants, and +1 is added to take into account particle $i$. Because the determination of the density $\rho_i$ at the particle location requires the $h_i$'s which are not known a priori, one usually takes the time derivative of equation (11) and substitute the continuity equation to yield:

$$\dot{h}_i \equiv \frac{dh_i}{dt} = \frac{1}{3} h_i \left( \frac{1}{N_i + 1} \frac{dN_i}{dt} + \vec{\nabla} \cdot \vec{v} \right). \qquad (12)$$

The traditional approach to ensure a constant number of neighbours is to set $dN_i/dt$ to zero. However, this does not prevent a slow numerical departure of the $N_i$'s from $N_o$ with time. Instead, the present code takes advantage of the $N_i$ term to correct such departures by setting:

$$\frac{dN_i}{dt} = \frac{N_o - N_i}{\eta \Delta t}, \qquad (13)$$

where $\eta > 1$ is a parameter to soften the correction over several time steps $\Delta t$ and avoid sharp changes in the forces. Equation (12) is then integrated along with the phase-space coordinates. The standard deviation of the neighbour numbers resulting from this procedure is generally only $\sigma(N_i) \sim 1.5$.

The initial conditions often lead to a large spread of the $N_i$'s. Therefore the simulations are started with a small $\Delta t$ allowing the $h_i$'s to automatically adjust without much evolution.

### (b) Neighbour search

In Friedli's original code, the search of the neighbours to each SPH particle is based on the 3D linked list method. The main steps are as follows: (i) the gas particles are sorted into increasing $x$, $y$ and $z$ coordinates, and by decreasing smoothing length $h_i$, (ii) each space dimension is divided into $N_x$ planes with the same number of gas particles between successive planes, (iii) a list of particles within each cell defined by this space subdivision is created, (iv) proceeding by decreasing $h_i$, the cells within $2h_i$ of each particle $i$ are localised, and (v) for all gas particles $j$ within these cells, the distance $r_{ij} \equiv |\vec{r}_j - \vec{r}_i|$ is derived and the particles $i$ and $j$ are considered as mutual neighbours if $r_{ij} < h_i + h_j$. This last reciprocity requirement ensures that the forces between pairs of particles are symmetric.

In the present code, this algorithm has been modified in two ways: the space subdivision is done only in the $x$ and $y$ dimensions (2D linked list), and we first test whether $z_{ij} \equiv |z_j - z_i| < h_i + h_j$ before computing $r_{ij}$, which is more time consuming because involving three multiplications. This reduces the CPU time for the search of neighbours by a factor $\sim 3$, mainly owing to the first of these changes, and this is true even for spherical distributions of particles. The algorithm is fastest when there is roughly one gas particle per cell on the average, i.e. when $N_x \approx \sqrt{N_{\text{gas}}}$.

## IV. INTEGRATOR

The basic requirements for an ideal time integrator are (i) an adaptative time-step to temporally resolve the gaseous shocks, (ii) a second order accuracy in the time step $\Delta t$, which is enough under particle noise, (iii) a precision similar to the time-reversible leap-frog algorithm for constant $\Delta t$, (iv) synchronised positions and velocities, (v) only one force evaluation per $\Delta t$, and (vi) a memory saving execution.

The adopted algorithm is a synchronised version of the leap-frog (e.g. Hut et al. 1995). At each time step, the positions and velocities of all particles and the smoothing lengths of the gas particles are modified

according to:

$$\vec{r}_i^{\,n+1} = \vec{r}_i^{\,n} + \vec{v}_i^{\,n}\Delta t^n + \frac{1}{2}\vec{a}_i^{\,n}(\Delta t^n)^2, \quad (14)$$

$$\vec{v}_i^{\,n+1} = \vec{v}_i^{\,n} + \frac{1}{2}(\vec{a}_i^{\,n} + \vec{a}_i^{\,n+1})\Delta t^n, \quad (15)$$

$$h_i^{n+1} = h_i^n + \frac{1}{2}(\dot{h}_i^n + \dot{h}_i^{n+1})\Delta t^n, \quad (16)$$

where the $\vec{a}_i$'s are the accelerations. Contrary to the statement in Fux (1999), the position and velocity part of the algorithm are both exactly reversible in time (Monaghan 2001, private communication). In collisionless $N$-body simulations and at constant $\Delta t$, this algorithm produces results very similar to the standard leap-frog algorithm. In particular, both algorithm conserve equally well the total energy and the total $z$-component of the angular momentum. However, the Runge-Kutta-Fehlberg algorithm (Fehlberg 1968) implemented in Friedli's original code leads to a significantly different evolution and to a much worse conservation of these quantities.

In simulations with gas, the pressure and viscous forces contributing to $\vec{a}_i^{\,n+1}$, as well as $\dot{h}_i^{n+1}$, depend on smoothing lengths and velocities which are not known a priori. To solve this problem, $\vec{a}_i^{\,n+1}$ and $\dot{h}_i^{n+1}$ are calculated with first order predictions of these quantities, which does not compromise the second order accuracy of $\vec{r}_i^{\,n+1}$, $\vec{v}_i^{\,n+1}$ and $h_i^{n+1}$.

The time step in PMDSPH is adaptive and its updating procedure is inspired from Friedli's code. After step $n$, the next time step $\Delta t^{n+1}$ is estimated from the condition that the maximum relative contribution per time step of the second order terms to the integrated quantities should not exceed a given tolerance $E_{\text{tol}}$. This condition, which is applied only to gas particles and is essentially driven by the smoothing lengths, is tested after step $n+1$ and, if not satisfied, the former values of the integrated quantities are restored and integrated again with a smaller $\Delta t^{n+1}$. The time step is also given an upper limit $\Delta t_{\text{o}}$ dictated by the Courant criterion.

Equations (15) and (16) and the step-rejection test impose to store the old values of all integrated quantities and related derivatives except the velocities of the non-gaseous particles, hence conflicting with requirement (vi). Otherwise, the algorithm satisfies all other requirements listed above.

## V.  APPLICATION TO THE MILKY WAY

Aiming a better understanding of the observed features in the HI and CO longitude-velocity diagrams within the Galactic bar region (Fig. 2), the code has been used to evolve a bar unstable axisymmetric model of the Milky Way. This initial model includes a stellar nucleus-spheroid, a double exponential stellar disc, a double Gaussian and linearly flaring gas disc, and a dark halo to ensure a flat rotation curve well beyond
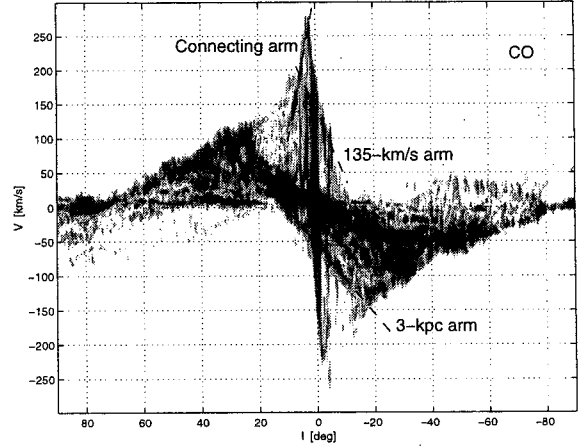


**Fig. 2.—** $^{12}$CO longitude-velocity diagram integrated over the range $|b| \leq 2°$ (from Dame et al. 2001). Some of the main features within the central few kpcs are also shown.

the solar circle, which is treated as a live component during the simulation (see Fux 1999 for details). The stellar and dark components are represented by over $1.4 \times 10^7$ particles, and the gas component by 150 000 SPH particles. The stellar and gas particles have the same mass to minimise two-body relaxation effects. The parameters of the gravitational double grid are set to $N_R \times N_\phi \times N_z = 62 \times 64 \times 242$, $M_z = 6$, $H_z = 60$ pc and $R_{\text{max}} = 50$ kpc. The sound speed for the gas in the simulation discussed here is $c_s = 10$ km s$^{-1}$ and its adiabatic index $\gamma = 5/3$. The SPH related parameters are $N_{\text{o}} = 35$, $\eta = 5$ and $N_x = 500$, and the time integration parameters $E_{\text{tol}} = 0.1$ and $\Delta t_{\text{o}} = 0.1$ Myr.

The simulation is first run keeping the gas component fixed to avoid an unrealistic concentration of gas in the centre while the bar is still growing, which owes to the absence of star formation in the code. The bar is formed after $\sim 1.4$ Gyr, with an in-plane axis ration $b/a \approx 0.6$. The gas is then gently released at $t = 2.4$ Gyr (for the case presented here), increasing gradually the non-axisymmetric part of the potential to its full value over half a rotation period of the bar, and the integration is carried out self-consistently to $t = 2.78$ Gyr.

The density centre of the bar oscillates around the centre of mass with an average amplitude of $\sim 300$ pc, and is closely tracked by a nuclear ring appearing in the gas component. The gas flow is asymmetric and remains non-stationary throughout the simulation, reproducing qualitatively the observed $\ell - V$ diagram only at specific times and thus suggesting a transient nature of the observed inner gas kinematics. Some mpeg animations, including live $\ell - V$ diagrams, are available at http://obswww.unige.ch/~fux.

Figure 3 shows a snapshot of the simulation where the gas reproduces well many of the observed features. One of the greatest success of this model is that it allows to identify the $\ell - V$ traces of the shock induced
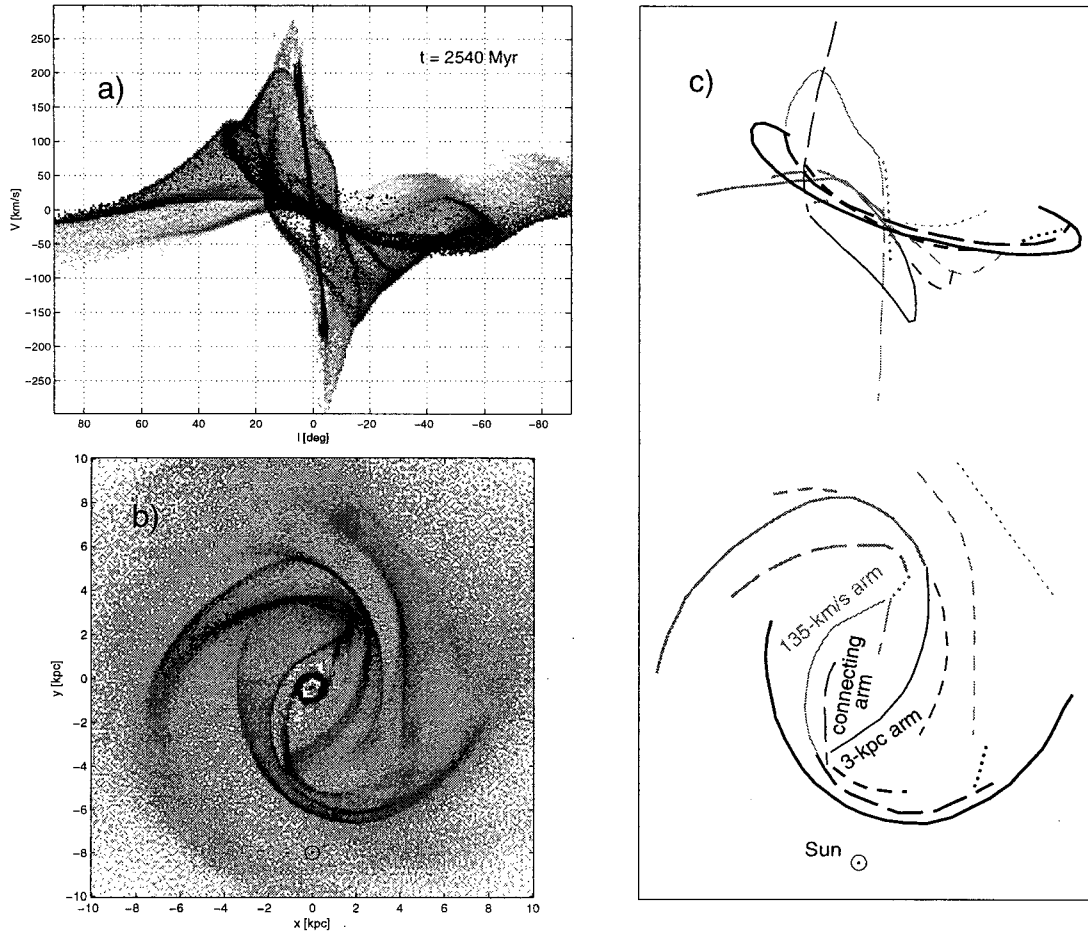
Fig. 3.— Selection of a model from the simulation which provides a good qualitative agreement to the observations (Fig. 2). a) $\ell - V$ distribution of the gas particles. b) Face-on view of the gas distribution, with the location of the observer indicated by the $\odot$ symbol. The bar inclination angle is $\varphi = 25°$ and the ratio of the corotation radius to the galactocentric distance of the observer is $R_{CR}/R_o = 0.55$. c) Link between the spiral arms in the $x - y$ plane and their $\ell - V$ traces.

gaslanes near the major axis of the Galactic bar, which are so often seen as prominent dustlanes in optical images of external barred galaxies. The near-side branch of these gaslanes corresponds to the connecting arm, and the far-side branch is predicted as a velocity elongated feature which is indeed apparent near $\ell = -4.5°$ in Fig. 2. Furthermore, the 3-kpc and the 135-km s$^{-1}$ arms are interpreted as the inner prolongations of disc spiral arms passing close to one end of the bar and joining by a large bow around the centre the gaslane on the other side of the bar. The substantial asymmetry in velocity of these arms at $\ell = 0$ is because they reach different depths in the central potential well.

The PMDSPH code and its single gravitational grid homologue are available by request to the author.

## ACKNOWLEDGEMENTS

## REFERENCES

Benz, W. 1990, in The Numerical Modelling of Nonlinear Stellar Pulsations, ed. J.R. Buchler, NATO ASI Ser. C 302, 269

Dame, T.M., Hartmann, D., & Thaddeus, P. 2001, ApJ 547, 792

Fehlberg, E. 1968, NASA Technical Report TR-R287

Friedli, D. 1992, Ph.D. Thesis 2553, Geneva Observatory, Geneva

Fux, R. 1999, A&A 345, 787

Gerhard, O. 2001, in Galaxy Disks and Disk Galaxies, eds. J.G. Funes, S.J. and E.M. Corsini, ASP conf. Ser. 230, 21

Hockney, R.W., & Eastwood, J.W. 1981, Computer Simulation Using Particles, McGraw-Hill, U.S.A.

Hut, P., Makino, J., & McMillan, S. 1995, ApJ 443, L93

Monaghan, J.J. 1992, ARA&A 30, 543

Pfenniger, D., & Friedli, D. 1993, A&A 270, 561